

# PanoFlow: Learning 360° Optical Flow for Surrounding Temporal Understanding

Hao Shi<sup>†1</sup>, Yifan Zhou<sup>†2</sup>, Kailun Yang<sup>3</sup>, Xiaoting Yin<sup>1</sup>, Ze Wang<sup>1</sup>, Yaozu Ye<sup>1</sup>, Zhe Yin<sup>4</sup>, Shi Meng<sup>5</sup>, Peng Li<sup>1</sup>, and Kaiwei Wang<sup>1</sup>

**Abstract**—Optical flow estimation is a basic task in self-driving and robotics systems, which enables to temporally interpret traffic scenes. Autonomous vehicles clearly benefit from the ultra-wide Field of View (FoV) offered by 360° panoramic sensors. However, due to the unique imaging process of panoramic cameras, models designed for pinhole images do not directly generalize satisfactorily to 360° panoramic images. In this paper, we put forward a novel network framework—PANOFlow, to learn optical flow for panoramic images. To overcome the distortions introduced by equirectangular projection in panoramic transformation, we design a *Flow Distortion Augmentation (FDA)* method, which contains radial flow distortion (FDA-R) or equirectangular flow distortion (FDA-E). We further look into the definition and properties of cyclic optical flow for panoramic videos, and hereby propose a *Cyclic Flow Estimation (CFE)* method by leveraging the cyclicity of spherical images to infer 360° optical flow and converting large displacement to relatively small displacement. PanoFlow is applicable to any existing flow estimation method and benefits from the progress of narrow-FoV flow estimation. In addition, we create and release a synthetic panoramic dataset *Flow360* based on CARLA to facilitate training and quantitative analysis. PanoFlow achieves state-of-the-art performance on the public OmniFlowNet and the fresh established Flow360 benchmarks. Our proposed approach reduces the End-Point-Error (EPE) on Flow360 by 27.3%. On OmniFlowNet, PanoFlow achieves an EPE of 3.17 pixels, a 55.5% error reduction from the best published result (7.12 pixels). We also qualitatively validate our method via an outdoor collection vehicle and a public real-world OmniPhotos dataset, indicating strong potential and robustness for real-world navigation applications. Code and dataset are publicly available at [PanoFlow](#).

**Index Terms**—Intelligent Vehicles, Scene Parsing, Optical Flow, Panorama, Scene Understanding, Synthetic Dataset.

## I. INTRODUCTION

This work was partly supported by Sunny Optical Technology (Group) Co. Ltd. This work was also supported in part by the National Natural Science Foundation of China (NSFC) under Grant No. 12174341, in part by the Federal Ministry of Labor and Social Affairs (BMAS) through the AccessibleMaps project under Grant 01KM151112, in part by the University of Excellence through the “KIT Future Fields” project, and in part by Hangzhou SurImage Technology Company Ltd. (Corresponding author: Kaiwei Wang.)

<sup>†</sup>H. Shi, X. Yin, Z. Wang, Y. Ye, P. Li, and K. Wang are with State Key Laboratory of Modern Optical Instrumentation, Zhejiang University, 310027 Hangzhou, China (email: haoshi@zju.edu.cn; xiaotingyin@zju.edu.cn; wangze0527@zju.edu.cn; yaozuye@zju.edu.cn; lipeng@zju.edu.cn; wangkaiwei@zju.edu.cn).

<sup>2</sup>Y. Zhou is with Multimedia Laboratory, Nanyang Technological University, 61 Nanyang Dr, Singapore 637335, Singapore (email: yifan.zhou@ntu.edu.sg).

<sup>3</sup>K. Yang is with Institute for Anthropomatics and Robotics, Karlsruhe Institute of Technology, 76131 Karlsruhe, Germany (email: kailun.yang@kit.edu).

<sup>4</sup>Z. Yin is with College of Computer Science and Technology, Zhejiang University, 310027 Hangzhou, China (email: pidandan@zju.edu.cn).

<sup>5</sup>S. Meng is with Data Intelligence Lab, Luokung Technology Corp., 100020 Beijing, China (email: mengshi@luokung.com).

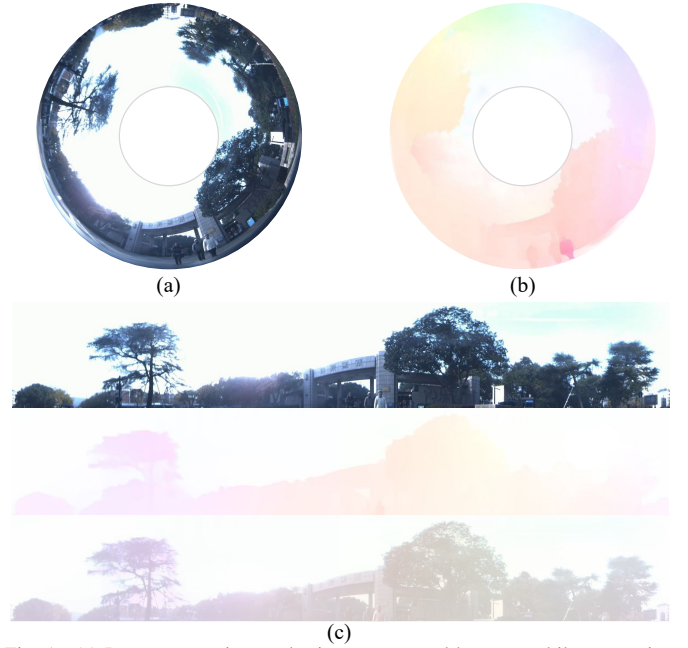


Fig. 1. (a) Raw panoramic annular image captured by our mobile perception system, (b)-(c) the proposed panoramic optical flow estimation on real-world surrounding view for 360° seamless scene temporal understanding.

OPTICAL flow estimation is one of the fundamental challenges for autonomous driving [1]–[5]. Flow estimation provides information about the environment and the sensor’s motion, leading to a temporal understanding of the world, which is vital for many robotics and vehicular applications, including scene parsing, image-based navigation, visual odometry, and SLAM [6]–[12]. With the development of spherical cameras [13], panoramic images are now more easily captured for 360° scene perception [14]–[16], and can better be integrated with LiDARs due to the similar projection model [17]. However, learning-based methods have always focused on traditional 2D images produced by pinhole projection model based cameras [18]–[20]. Models designed for a camera with narrow Field-of-View (FoV) are usually sub-optimal for a comprehensive understanding. Coupling them with 360° LiDARs would also directly lead to inherent and domain adaptation problems [21]. Thus, the ability to infer optical flow of a camera’s complete surrounding has motivated the study of 360° flow estimation.

Unlike classical linear images, panoramic contents often suffer from severe distortions due to the equirectangular projection (ERP) of spherical cameras [22]. An object will deform to varying degrees at different latitudes in panoramic images, making flow estimation more difficult between the

target image and the attended image. Another critical issue lies in the cyclicity of spherical boundaries, which means there is more than one path from the source point to the target point, and usually there is one shorter and one longer path [23]. The two routes together form a great circle on the sphere. In other words, the geometric meanings of the two routes are equivalent. However, traditional learning-based models cannot track pixels moving outside the image boundary, and therefore have no choice but to infer the harder long-distance motion vector, leading to less satisfactory estimation.

To tackle these issues, we introduce a new panoramic flow estimation framework—PANOFLOW, to directly estimate dense flow field from panoramic images. We implement PanoFlow on two different state-of-the-art optical flow networks [19], [20] to verify the generality of the proposed framework. We present the first, to the authors’ best knowledge, a *Flow Distortion Augmentation (FDA)* method, that is built on the insight of the distortion induced by ERP, to enhance robustness against deformations in panoramic images. While distortion augmentation is used in panoramic scene parsing [24], [25], it has not been investigated in optical flow estimation, as optical flow is a 2D vector, which incurs further challenges. Unlike traditional geometric augmentation methods that deal with constant properties, distortion augmentation of optical flow is non-trivial, which has to consider the variation of optical flow because the initial and terminal points of the flow would be distorted to different extent. By projecting participating images (attended- and target images) and flow ground truth onto the distortion field, we improve the model’s ability to generalize to deformed regions.

We put forward two variants of flow distortion augmentation: radial flow distortion (FDA-R) and equirectangular flow distortion (FDA-E). Although FDA-E is consistent with the distortion introduced by general ERP, given the smaller FoV of the pinhole dataset, the number of pixels that really participate in supervision is reduced. We therefore also explore the role of FDA-R in overcoming ERP distortion. We found that although their deformed models are not exactly identical, FDA-R also improves the network’s ability to handle distorted regions. From another distortion-adaptive perspective, we further propose to address the distortion by replacing the first layer of the encoder with a deformable convolution layer [26]. The proposed FDA and the deformable convolution empower the model to handle characteristic panoramic image distortions and robustify flow estimation. As a novel data augmentation method, FDA is a plug-and-play module for any learning-based optical flow network.

Furthermore, we give a standard definition of cyclic optical flow suitable for panorama video stream, analyze the properties of cyclic optical flow and compare it with classical optical flow. We then design a *Cyclic Flow Estimation (CFE)* method based on the previous insight to leverage the cyclicity of panoramic images, and convert long-distance estimation to a relatively short-distance estimation. CFE well relieves the stress of the model in large displacement estimation, enabling the model to focus on local fine-grained optical flow estimation. CFE is a general optical flow estimation method and thus can benefit from the advances of narrow-FoV flow estimation

methods. Interestingly, both quantitative and qualitative results show that, compared to the previous best method [23] which estimates on the cubemap plane and the icosahedral tangent plane iteratively, the CFE method is simple, yet very effective. We also calculate the distribution of the accuracy change with the horizontal FoV before and after using the CFE method, and discover that CFE can significantly improve the optical flow estimation accuracy near the panorama vertical boundary, which is a unique difficulty of panoramic flow estimation.

In addition, to overcome the lack of available panoramic training data and to foster research on 360° understanding, we establish and release a new synthetic panoramic flow estimation benchmark of street scenes—*Flow360*. We generate the dataset via the CARLA simulator [27]. Flow360 consists of 6,400 color images, optical flow, and pixel-level semantic ground truth, providing an environment similar to the real world, thanks to dynamic weather, diverse city street scenes, and different types of vehicles. We use this dataset for learning to infer flow from panoramic content. We also analyze the ground-truth quality of existing optical flow datasets [22], [23], [28] when only forward optical flow is given, and determine our evaluation datasets according to the observations.

We conduct extensive quantitative experiments on the established Flow360 benchmark. Compared with the previous best model, the End-Point-Error (EPE) of PanoFlow on this dataset reduces by 27.3%. Further, the EPE of our approach on the public OmniFlowNet dataset [22] is reduced by 55.5% compared with the best published results (3.34 pixels vs. 7.12 pixels). Moreover, a comprehensive set of ablation experiments demonstrates the effectiveness of the proposed FDA and CFE methods. We additionally conduct qualitative analysis on the public real-world OmniPhotos dataset [29] to validate our approach in real-world surrounding perception. To further demonstrate the generalization ability of PanoFlow, We also assemble an outdoor data collection vehicle installed with a Panoramic Annular Lens (PAL) system. As shown in Fig. 1, PanoFlow gives sharp and clean omnidirectional optical flow estimation for real-world surrounding scenes.

In summary, our main contributions are as follows:

- We present a rigorous theoretical definition of 360° optical flow.
- We introduce *flow distortion augmentation*, a new data augmentation method for optical flow networks, which can help models learn to capture the motion cues even on deformed regions.
- We propose a generic *cyclic flow estimation* method, which can transform large- to relatively short displacement estimation based on the geometric nature of consecutive panoramas.
- We generate *Flow360*, a new publicly available panoramic dataset that consists of diverse synthetic street scenes, providing both pixel-level flow- and semantic ground truth. We also assess ground-truth quality of existing panoramic flow datasets.
- Our entire framework PANOFLOW achieves state-of-the-art performance on the established Flow360 benchmark and the public OmniFlowNet dataset.

- PanoFlow demonstrates strong generalization ability both on the public real-world OmniPhotos dataset and our captured outdoor panoramic video streams.

## II. RELATED WORK

### A. Learning-based Optical Flow Estimation

The classical optical flow estimation approaches [30], [31] use variational approaches to minimize energy based on brightness constancy and spatial smoothness. Since the advent of FlowNet [32], some other works based on Convolutional Neural Networks (CNNs) [33]–[44] have appeared. Besides, there are also some self-supervised approaches [45], [46] to learn optical flow with occlusions. Most of these methods are normally designed to work with pinhole cameras capturing a limited imaging angle.

FlowNet [32] first treats optical flow estimation as a learning problem. In order to further improve the accuracy of optical flow, FlowNet2.0 [47] introduces image warping between multiple cascaded FlowNets. Due to the large model size of FlowNet2.0 [47], many methods have been proposed to simultaneously improve the optical flow accuracy and reduce the model size. Among them, PWC-Net [18] combines classical optical flow estimation principles including pyramid processing, image warping, and cost volumes with learning. LiteFlowNet2 [48] draws on the idea of data fidelity and regularization in the classical variational optical flow method. RAFT [19] iteratively update optical flow fields using multi-scale 4D correlation volumes. To better apply optical flow estimation to autonomous driving systems, CSFlow [20] proposes a new optical flow deep network architecture composed of Cross Strip Correlation module (CSC) and Correlation Regression Initialization module (CRI). Moreover, FlowFormer [49] replaces the CNN-based backbone in the RAFT architecture with a transformer-based backbone, which further improves the accuracy of optical flow estimation while increasing the number of parameters by three times. In contrast, PanoFlow is a panoramic optical flow framework that can be adapted to any optical flow network with an encoder-decoder architecture.

### B. Optical Flow Estimation beyond the FoV

With the arrival on the market of the increasingly affordable, portable, and accurate panoramic cameras, 360° flow estimation is in urgent need, that can provide a wide-FoV temporal understanding, for which some methods based on deep learning are developed. LiteFlowNet360 [50] is designed as a domain adaptation framework to cope with inherent distortion in 360° videos caused by the sphere-to-plane projection. They employ incremental transformation of convolutional layers in feature pyramid networks to reduce network growth size and computational costs combining data augmentation and self-supervised learning with target-domain 360° videos. OmniFlowNet [22] is built on a CNN model that specializes in perspective images and then applied to omnidirectional ones without training on new datasets, whose convolution operation is unified with equirectangular projection, outperforming the original network. The projection from the 360° image to the ERP image is a nonlinear mapping, and the distortion caused

by this will affect the 360° optical flow estimation, thus Yuan *et al.* [23] propose a 360° optical flow estimation method based on tangent images, including dozens of estimations and refinements on both icosahedron and cubemap panoramas. Differing from these works, we tackle image distortions and object deformations that appear across the entire 360° scenes and leverage the cyclicity of consecutive omnidirectional data for enhancing panoramic optical flow estimation.

### C. Optical Flow and Panoramic Perception Datasets

Panoramic datasets are needed in a wide variety of application areas, including depth estimation [51]–[53], scene segmentation [54]–[56], and optical flow estimation [22], [23], [28]. Stanford2D3D [57] is a large-scale indoor spaces dataset that consists of both regular and panoramic data with instance-level semantic annotations. The 360D dataset [21] reuses released large-scale 3D datasets and re-purposes them to 360° via rendering for dense depth estimation. PASS [24] presents a panoramic annular semantic segmentation framework with an associated dataset for credible evaluation. DensePASS [58] introduces a dataset with both labeled and unlabeled 360° images for benchmarking panoramic semantic segmentation from a perspective of unsupervised domain adaptation. KITTI-360 [59] is collected with perspective stereo cameras, a pair of fisheye cameras, and a laser scanning unit for enabling 360° perception. WoodScape [60] comprises of multiple surround-view fisheye cameras and multiple tasks like segmentation and soiling detection. The OmniScape dataset [61] includes semantic segmentation, depth map, intrinsic parameters of the cameras, and the dynamic parameters of the motorcycle. The Waymo Open dataset [62] is a labeled panoramic video dataset for panoptic image segmentation.

Aiming at improving the accuracy of optical flow estimation, OmniFlow [63] is a synthetic omnidirectional human optical flow dataset with images of household activities with a FoV of 180°. OmniFlowNet [22] renders a test set of panoramic optical flow only for validation, using simple geometric models based on Blender. Replica360 [23] implements an ERP camera model for the Replica rendering pipeline [64] and contains ground-truth optical flow in the equirectangular format for validation. SynWoodScape [28] is a synthetic fisheye surround-view dataset with ground truth for pixel-wise optical flow and depth estimation. OmniPhotos [29] is a fast 360° panoramic VR photography method with an released outdoor dataset, but it cannot obtain the ground truth of optical flow. We note that, until now, there is neither a dataset for omnidirectional images targeting at outdoor complex street scenes, nor a dataset covers 360° that can be used for training and evaluation. The present paper seeks to fill this gap, by proposing a virtual environment, in which one car with panoramic camera drives under the assumption that pedestrians and vehicles move according to traffic rules. Tab. I relates and summarizes current panoramic datasets that contain ground-truth optical flow. A detailed analysis of the ground-truth quality of optical flow will be unfolded in Sec. IV.



TABLE I  
COMPARISON OF EXISTING PANORAMIC DATASETS FOR OPTICAL FLOW ESTIMATION.

Dataset	Train/Test Split	Groundtruth Quality	ERP format	Resolution	Semantics	Outdoor	Dynamic Weathers	Frames
OmniFlowNet Dataset [22]	✗	high	✓	$384 \times 768$	✗	✓	✗	1500
Replica360 [23]	✗	medium/low	✓	$640 \times 1280$	✗	✗	✗	954
SynWoodScape [28]	✗	medium/low	✗	<b><math>966 \times 1280</math></b>	✓	✓	✗	500
Ours (Flow360)	✓	high	✓	$512 \times 1024$	✓	✓	✓	<b>6400</b>

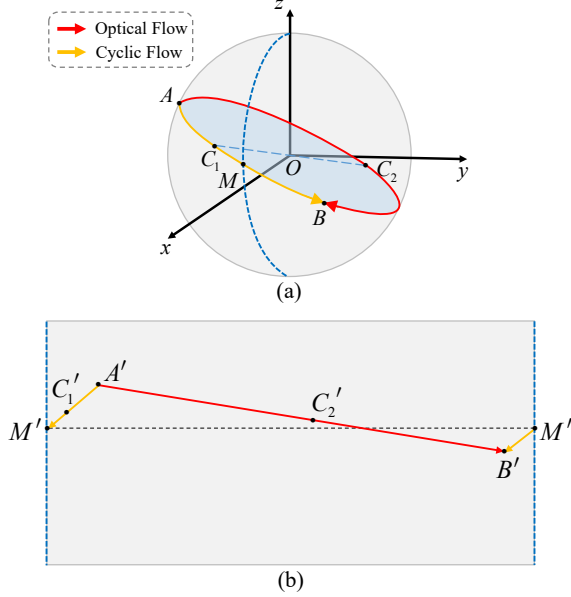


Fig. 2. Schematic diagram of cyclic optical flow. (a) The optical flow and the cyclic optical flow form a complementary great circle on the spherical coordinate system, (b) The cyclic optical flow on an equirectangular image has a relatively small displacement and spans the horizontal boundaries of the panorama.

### III. PANOFlow: PROPOSED FRAMEWORK

#### A. Definition of 360° Optical Flow

The spherical image does not contain any boundaries, and the coordinates are continuous in any direction on the image [22]. However, a boundary parallel to the meridian is naturally introduced in the process of unfolding the spherical image into an equirectangular image as shown in Fig. 2. Given any point  $A$  on the sphere, which moves to another point  $B$  after time  $t$ . Due to the cyclic nature of the sphere itself, there are actually infinite arc trajectories between these two points. Now we only consider two arcs  $\widehat{AC_1B}$  and  $\widehat{AC_2B}$  whose range are less than the circumference of the great circle, where  $C_1$  and  $C_2$  are the vertices of the arcs at both ends, respectively. It is easy to find that these two arcs together form a great circle on the sphere. In the process of spherical unfolding, we can map these two points to  $A'$  and  $B'$  on the equirectangular image plane  $I_e \in \mathbb{R}^{H \times W}$ , respectively, according to the forward ERP:

$$\begin{cases} x = L(\phi - \phi_0)\cos\theta_1, \\ y = L(\theta - \theta_0), \end{cases} \quad (1)$$

where  $\theta \in (-\frac{1}{2}\pi, \frac{1}{2}\pi)$ ,  $\phi \in (-\pi, \pi)$  are the unit spherical coordinate pitch and yaw,  $\phi_0, \theta_0$  are central meridian and central

parallel, respectively.  $\theta_1$  are the standard parallels.  $L$  is the scaling factor. Therefore, the cyclicity of a great circle on the sphere, is reflected in the cyclicity of the vertical boundary on the equirectangular image:

$$\delta x = L\cos\theta_1 \cdot (\delta\phi \bmod 2\pi), \quad (2)$$

where  $(a \bmod b)$  indicates  $a$  modulo  $b$ . Considering a pair of an attended image and a target image, pixels moving out the image boundary on one side will locate to the other side of the image. Thus, there are two 2D motion vectors that connect the source and target points: one is connected along the interior of the equirectangular image, whereas the other points outside the image boundaries. These two flow vectors together form a great circle on the spherical image, one shorter and one longer.

For the classical definition of optical flow, given two frames of sequence equirectangular RGB images  $I_1$  and  $I_2$ , we estimate the dense motion vector  $(u, v)$  from each pixel  $(x, y)$  of  $I_1$  to each pixel  $(x', y')$  of  $I_2$ , that is, the optical flow field  $\mathbf{V}$ , which gives the per-pixel mapping relationship between the source and target. However, classical optical flow cannot track pixels that move outside the image boundaries, and cannot reflect the boundary circulation of panoramic optical flow. Thus, we define 360° optical flow  $\mathbf{V}_{360}$  as the shortest path from source to target along the great circle between them, which naturally limits the scalar value of lateral optical flow to  $u \leq 180^\circ$ . For ground-truth flow field  $\mathbf{V}_{GT}(\mathbf{x}) = (u, v)$  at pixel index  $\mathbf{x}$  of equirectangular images, we can easily convert the optical flow to 360° flow:

$$\mathbf{V}_{360}(\mathbf{x}) = \begin{cases} (u - W, v), & \frac{1}{2}W < u \leq W; \\ (u + W, v), & -W \leq u < -\frac{1}{2}W; \\ (u, v), & \text{others.} \end{cases} \quad (3)$$

Given a dense cyclic optical flow field  $\mathbf{V}_{360}$ , we can always find the mapping point  $(x', y')$  on  $I_2$  from every pixel  $(x, y)$  on  $I_1$ , i.e., cyclic optical flow maintains the temporal continuity of classical optical flow, which can be used to align temporal features when considering boundary cyclicity.

#### B. Data Augmentation with Flow Distortion

In optics, distortion is a map projection which makes the straight lines distorted. Relative to perspective images, the equirectangular transformation can be regarded as a kind of distortion. The models trained on perspective images suffer from the distortion on equirectangular images. To adapt the models to this distortion, we put forward to perform *Flow Distortion Augmentation (FDA)* on the training samples as a novel data augmentation method.

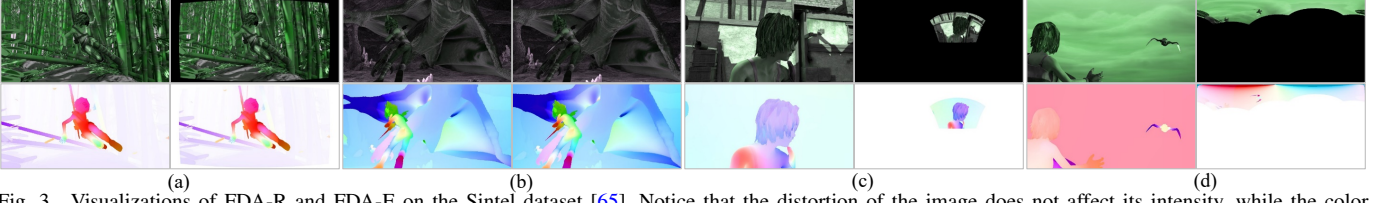


Fig. 3. Visualizations of FDA-R and FDA-E on the Sintel dataset [65]. Notice that the distortion of the image does not affect its intensity, while the color of the optical flow changes with the modulus. (a) Barrel distortion in FDA-R, (b) Pillow distortion in FDA-R, (c) Low latitude distortion in FDA-E, (d) High latitude distortion in FDA-E.

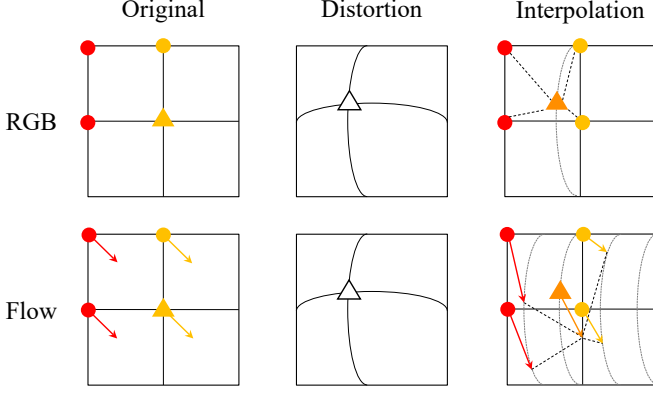


Fig. 4. The comparison between RGB image distortion and optical flow distortion. Since the optical flow of grid points has also been modified during distortion, it should be calibrated before interpolation.

The distortion of flow is a non-trivial task comparing to general image distortion (Fig. 4). For the properties that adhere to the pixels (e.g., RGB or depth), their values would not be modified during distortion. However, the initial and terminal points of optical flow would both be distorted during distortion. To estimate the exact optical flow of a distorted frame, we should calibrate the optical flow of its grid points before interpolation. Given an undistorted initial point  $\mathbf{x}_u = (x_u, y_u)$ , the flow field  $\mathbf{V}_u$ , and a coordinate distortion function  $F$  that maps a distorted coordinate to a calibrated coordinate, the calibrated flow field  $\mathbf{V}_c$  can be obtained by:

$$\begin{cases} \mathbf{V}_c(\mathbf{x}_d) = F'(\mathbf{x}_u + \mathbf{V}_u(\mathbf{x}_u)) - F'(\mathbf{x}_u), \\ \mathbf{x}_d = F'(\mathbf{x}_u), \end{cases} \quad (4)$$

where  $\mathbf{x}_d = (x_d, y_d)$  is the distorted coordinate and  $F'$  is the inversion function of  $F$ . There are multiple choices for the coordinate distortion function  $F$ . In this work, we consider radial distortion and equirectangular distortion, both resulting a remarkable enhancement, which will be discussed in Sec. V-C. We use the following mapping function  $F_r : F(\mathbf{x}_u) \rightarrow \mathbf{x}_d$  to model the radial distortion:

$$\begin{cases} x_d = P(r)(x_c + (x_u - x_c)), \\ y_d = P(r)(y_c + (y_u - y_c)), \end{cases} \quad (5)$$

where  $(x_c, y_c)$  is the distortion center (the intermediate point of image by default).  $P(x) = x + k_2 x^2 + k_4 x^4$  is a polynomial and  $r$  is the Euclidean distance from  $(x_u, y_u)$  to  $(x_c, y_c)$ . In practice, we set  $k_2 \sim U(-10^{-6}, 10^{-6})$ ,  $k_4 \sim U(-10^{-14}, 10^{-14})$ , which are empirically set and achieve reasonable augmentation effects for images of different resolutions.

For equirectangular distortion  $F_e : F(\mathbf{x}_u) \rightarrow \mathbf{x}_d$ , we transform the coordinates via spherical coordinate system. We

first map  $\mathbf{x}_u$  on equirectangular image to  $\mathbf{x}_s = (x_s, y_s, z_s)$  on unit sphere by:

$$\begin{cases} x_s = \sin \frac{\pi y_u}{H} \cos \frac{2\pi x_u}{W}, \\ y_s = \sin \frac{\pi y_u}{H} \sin \frac{2\pi x_u}{W}, \\ z_s = \cos \frac{\pi y_u}{H}, \end{cases} \quad (6)$$

we then apply random rotation to  $\mathbf{x}_s$  by  $\mathbf{x}_s^T \leftarrow R_z R_y \mathbf{x}_s^T$ , where  $R_z$  and  $R_y$  are rotation matrices about z-axis and y-axis. Finally, we transform  $\mathbf{x}_s$  to perspective coordinate by:

$$\begin{cases} x_d = \frac{W}{2 \tan \frac{\theta_h}{2}} \frac{y_s}{x_s} + \frac{W}{2}, \\ y_d = \frac{H}{2 \tan \frac{\theta_v}{2}} \frac{z_s}{x_s} + \frac{H}{2}, \end{cases} \quad (7)$$

where  $\theta_h, \theta_v$  are the horizontal and vertical FoV of the perspective image drawn from  $U(\frac{\pi}{3}, \frac{2}{3}\pi)$  respectively.

The visualizations of FDA-R and FDA-E are shown in Fig. 3. Notice that the color of the optical flow changes with the distortion, which is due to that the vector distortion affecting the modulo value of the optical flow. The deformation of FDA-E is homogeneous with that introduced by ERP, while the deformation introduced by FDA-R is radially variable. However, due to the limited FoV of pinhole images, the number of available supervision pixels in FDA-E is actually reduced compared to FDA-R, thus it is necessary to explore the effects of two different optical flow distortion techniques on the distortion robustness of the model. It is verified that FDA improves the adaptation of model by introducing the distorted images to the training data. The ablation experiment of FDA is comprehensively discussed in Sec. V-C.

### C. Training with Deformable Receptive Field Encoder

Unlike pinhole images, equirectangular images suffer from severe geometric distortions in panoramic dense prediction [21], [24]. While our flow distortion augmentation helps address the deformations from the perspective of training data, classical CNN-based encoders are still limited by the fixed geometry of the convolution kernels, and has insufficient learning ability for deformable features. Therefore, we propose to replace the first convolutional layer of the encoder with deformable convolution [26] when dealing with 360° contents, endowing the model with a more flexible receptive field. Given a deformable convolution kernel, we extract features at  $K$  sampling locations, the weight and grid-specified offset at the  $k$ -th location are denoted by  $w_k$  and  $g_k$ , respectively. In our practice, we replace the feature encoder and context encoder with two deformable convolution layers with a kernel size of  $7 \times 7$ , thus the kernel is defined with  $K=49$  and  $g_k \in \{(-3, -3), (-3, -2), \dots, (0, 0), \dots, (3, 2), (3, 3)\}$ .

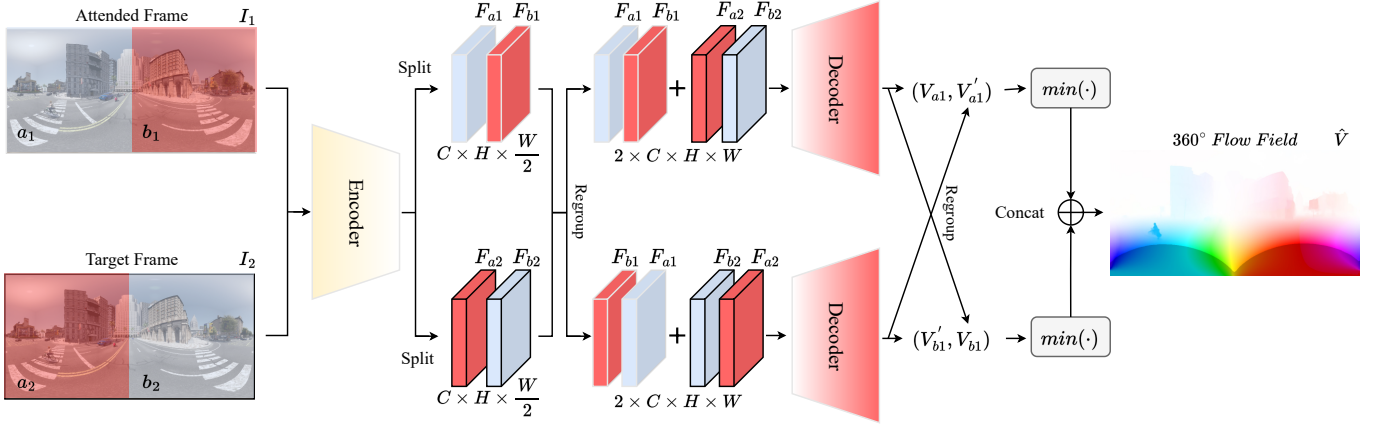


Fig. 5. *Cyclic Flow Estimation*. Partitioned feature maps are extracted from the encoder of the attended frame and the target frame. According to the cyclicity of the left and right boundaries of a panoramic image, the features extracted via the encoder, are regrouped into two feature pairs and sent to the decoder to obtain the complementary optical flow field. The 360° flow can finally be obtained via  $\min(\cdot)$  operations.

The distortion-aware features  $F_d$  at each position  $g_0$  can be obtained via:

$$F_d(g_0) = \sum_{k=1}^K w_k \cdot I(g_0 + g_k + \Delta g_k) \cdot \Delta o_k, \quad (8)$$

where  $I \in \mathbb{R}^{H \times W}$  is the panorama input,  $\Delta g_k$  and  $\Delta o_k$  are learnable offset and modulation scalar respectively, which are inferred via another convolutional layer. In Sec. V-C, we will show that the use of deformable receptive field encoder further enhances the robustness of the model to distorted images.

#### D. Inference with Cyclic Flow Estimation

In order to directly infer 360° cyclic flow from equirectangular contents, and relieve the stress of the model in long-distance displacement estimation, we introduce a *Cyclic Flow Estimation (CFE)* method based on the geometric nature of panoramas. The structure of CFE is shown in Fig. 5. CFE exploits the cyclicity of the left and right boundaries of equirectangular images, and it is compatible with any optical flow network based on an encoder-decoder structure, e.g., RAFT [19] or CSFlow [20].

Specifically, we first use a convolutional network as the encoder  $e(\cdot)$  to extract features  $F_1, F_2 \in \mathbb{R}^{C \times H \times W}$  from the input two frames of equirectangular images  $I_1, I_2 \in \mathbb{R}^{3 \times h \times w}$ . Then, the features are split along the horizontal centerline into  $F_{a1}, F_{b1} \in \mathbb{R}^{C \times H \times \frac{W}{2}}$  and  $F_{a2}, F_{b2} \in \mathbb{R}^{C \times H \times \frac{W}{2}}$ , respectively. We regard the process of feature encoding as rigid, that means, we should obtain exactly the same features for the same image input. Therefore, when swapping the left and right regions of the input image, the resulting feature maps should also be approximately left-right swapped. Based on the above observations, we can regroup the feature maps as two feature pairs  $P_1, P_2 \in \mathbb{R}^{2 \times C \times H \times W}$ :

$$\begin{cases} P_1 = \{F_{a1} \oplus F_{b1}, F_{a2} \oplus F_{b2}\}, \\ P_2 = \{F_{b1} \oplus F_{a1}, F_{b2} \oplus F_{a2}\}. \end{cases} \quad (9)$$

where  $\oplus$  means a concatenate operation. Since the RAFT structure [19] contains an additional context encoder  $c(\cdot)$ , the

context feature maps  $C_{a1}, C_{b1} \in \mathbb{R}^{C \times H \times \frac{W}{2}}$  extracted from  $I_1$  should also be regrouped into  $P_{c1}, P_{c2} \in \mathbb{R}^{C \times H \times W}$ :

$$\begin{cases} P_{c1} = \{C_{a1} \oplus C_{b1}\}, \\ P_{c2} = \{C_{b1} \oplus C_{a1}\}. \end{cases} \quad (10)$$

We then stack the feature pairs with context respectively, which will be further sent to the decoder  $d(\cdot)$ . The decoder will estimate two flow fields  $\mathbf{V}, \mathbf{V}' \in \mathbb{R}^{2 \times h \times w}$ . The flow estimations are split along the horizontal centerline into  $\mathbf{V}_{a1}, \mathbf{V}_{b1} \in \mathbb{R}^{2 \times h \times \frac{w}{2}}$  and  $\mathbf{V}'_{a1}, \mathbf{V}'_{b1} \in \mathbb{R}^{2 \times h \times \frac{w}{2}}$ . Assuming that the estimation is unbiased, for any pixel  $(x, y)$  in area  $a$ , we consider that  $\mathbf{V}_{a1}(x, y)$  and  $\mathbf{V}'_{a1}(x, y)$  form a pair of complementary optical flows end to end, and these two 2D motion vectors together form a great circle on the sphere. The same is true for area  $b$ . According to our definition of 360° optical flow, the final 360° flow field  $\hat{\mathbf{V}}$  is obtained:

$$\hat{\mathbf{V}} = \min(\mathbf{V}_{a1}, \mathbf{V}'_{a1}) \oplus \min(\mathbf{V}'_{b1}, \mathbf{V}_{b1}). \quad (11)$$

We emphasize again that CFE is a generic flow estimation method based on the assumption that the encoding process should be rigid, which can replace the large displacement estimation with the small displacement estimation when dealing with panoramic contents. According to our analysis of the geometric nature of consecutive panoramic frames in Sec. III-A, CFE is able to cope with the intrinsically most difficult part of long-range cyclic estimation in panoramic optical flow, without having to estimate dozens of times on the tangent plane of the regular polyhedron like the previous method [23]. Considering that large displacement estimation is much more challenging for the model, CFE can significantly enhance the prediction reliability. With the proposed CFE method, we eliminate redundant encoding calculations, and ensure computational efficiency while accurately estimating 360° optical flow. Another naive idea is to use circular convolutions to replace classical convolutional layers. However, we will show in ablation studies (Sec. V-C) that this method only has a limited circularity for cyclic flow, and thus it is not suitable for panoramic flow estimation.



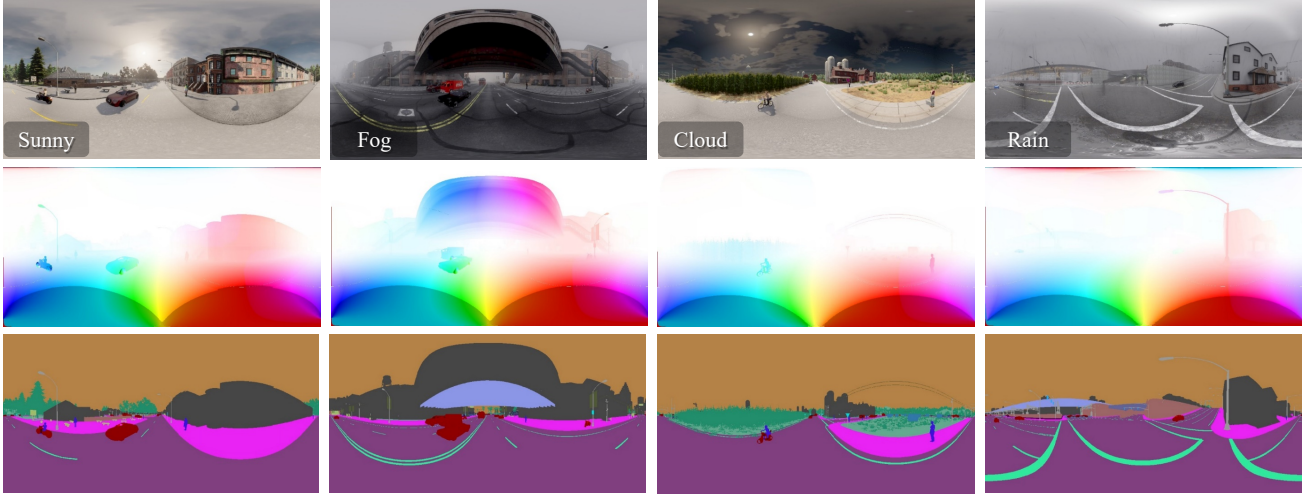


Fig. 6. From up to down: color images, optical flow, and semantics. The proposed *Flow360* dataset consists of 8 various city maps in four weathers: sunny, fog, cloud, and rain. We collect 100 consecutive panoramic images at each random position, resulting in a total of 6,400 frames with a resolution of  $512 \times 1024$ , each with optical flow ground truth and semantic labels, which can be used for training and evaluation. Since the flow field of panoramic images usually contains large displacement that interferes with visualization and fades colors, we modified the visualization method of optical flow based on [66], and lowered the color saturation of optical flow greater than the threshold. Please refer to our open-source documentation for details.

#### IV. FLOW360: ESTABLISHED SYNTHETIC DATASET

End-to-end learning of deep neural networks requires a large amount of annotated ground truth data. Although for pinhole cameras this can be partly resolved by using scanning LiDARs and multiple sensors [67], [68], such an approach is unpractical for  $360^\circ$  images, considering that panoramic camera and LiDAR will block each other and have a large divergence in their resolutions. In addition, the point cloud data given by LiDARs is sparse, thus it is difficult to obtain dense ground-truth values of optical flow in the real world. Even when these flaws are patched using algorithms during acquisition, additional errors are still introduced. On the other hand, synthetic datasets are popular for learning flow estimation due to the lack of real-world training data [32], [65], [69]. Extensive investigations have demonstrated that generalization from synthetic- to real scenes is feasible for optical flow tasks [19], [20], [70].

**Flow360 dataset:** We notice that there is a lack of an open panoramic optical flow dataset that can be used for training and credible numerical evaluation. Therefore, we advocate to generate a dataset with ground-truth flow by synthesizing both the color image and flow via the CARLA simulator [27]. Specifically, we use eight open-source maps given by CARLA. Our virtual collection vehicle contains 6 pinhole color cameras, 6 pinhole optical flow cameras, and 6 pinhole semantic cameras, all of which have a FoV of  $90^\circ \times 90^\circ$ , are in the same spatial viewpoint and keep synchronized timestamps. Taking color images as an example, six orthogonal viewing angles are obtained to form a cubemap panorama  $\{I_f, I_r, I_b, I_l, I_u, I_d\} \in \mathbb{R}^{h \times w}$ , including front, right, back, left, top, and bottom view. We can then acquire the equirectangular image  $I_e \in \mathbb{R}^{H \times W}$  with a FoV of  $180^\circ \times 360^\circ$  by using a cubemap-to-equirectangular algorithm. Given four horizontally views  $\{I_f, I_r, I_b, I_l\}$  of the cubemap format, we can calculate their corresponding coordinates  $(x, y)$  on the equirectangular image plane:

$$\begin{cases} x &= \frac{W}{2} \cdot \tan(\phi - m\frac{\pi}{2}), \\ y &= -\frac{H}{2} \cdot \frac{\tan\theta}{\cos(\phi - m\frac{\pi}{2})}, \end{cases} \quad (12)$$

where the view index  $m = \{1, 2, 3, 4\}$ ,  $\theta \in (-\frac{1}{2}\pi, \frac{1}{2}\pi)$ ,  $\phi \in (-\pi, \pi)$  are the angular coordinates. For the upper and lower views  $\{I_u, I_d\}$ :

$$\begin{cases} x &= \frac{W}{2} \cdot \tan(\frac{\pi}{2} - \theta) \sin(\phi), \\ y &= \frac{H}{2} \cdot \tan(\frac{\pi}{2} - \theta) \cos(\phi + n\pi), \end{cases} \quad (13)$$

where the view index  $n = \{0, 1\}$ . We use a tracing renderer to render our dataset by placing these pinhole cameras at a random position  $P \in \mathbb{R}^3$  in the scene. For each map, we augment the dataset by changing weather, including *sunny* (62.5%), *cloud* (12.5%), *fog* (12.5%), and *rain* (12.5%) to form Flow360 and assess the robustness of optical flow estimation in various conditions. In order to ensure a good diversity of the synthetic data, we only gather 100 frames with a frame rate of 30Hz for each position. Considering the unreliable optical flow at infinity such as that on points in the sky, we additionally provide ground-truth values of pixel-wise semantic segmentation for selection, which could also be beneficial for panoramic semantic understanding tasks [24], [25]. The semantic labels follow CARLA's setting (Fig. 6). Overall, Flow360 provides 6,400 panoramic images of diverse street scenes, each with ground truth of both optical flow and semantic labels.

**Photoconsistency analysis:** As shown in Tab. I, we compare the existing panoramic optical flow datasets. SynWoodScape [28], OmniFlowNet [22], and Replica360 [23] are three small datasets for evaluating panoramic optical flow. Due to their small size, they are not suitable for the training of neural network based methods. We further explore the photoconsistency [66] by introducing photometric error (PE) and warped photometric error (WPE) to evaluate the ground-truth optical flow quality of the dataset when only forward flow is given:

$$PE = \frac{1}{HW} \sum_{\mathbf{x}} |I_1(\mathbf{x}) - I_2(\mathbf{x})|, \quad (14)$$

$$WPE = \frac{1}{HW} \sum_{\mathbf{x}} |I_1(\mathbf{x} + \mathbf{V}_{GT}(\mathbf{x})) - I_2(\mathbf{x})|, \quad (15)$$

TABLE II  
GROUND-TRUTH QUALITY ANALYSIS OF OPTICAL FLOW DATASETS.

Modal	Dataset	PE	WPE	Diff.	GT Quality
Perspective	FlyingChairs [32]	23.35	12.43	↑ 46.8%	high
	FlyingThings [69]	25.57	19.26	↑ 24.7%	high
	MPI-Sintel [65]	13.93	7.12	↑ 48.9%	high
Panorama	SynWoodScape [28]	49.56	49.60	↓ 0.08%	medium/low
	OmniFlowNet [22]	8.47	5.75	↑ 32.1%	high
	Replica360 [23]	19.76	18.63	↑ 5.7%	medium/low
	Ours (Flow360)	5.96	3.07	↑ 48.7%	high

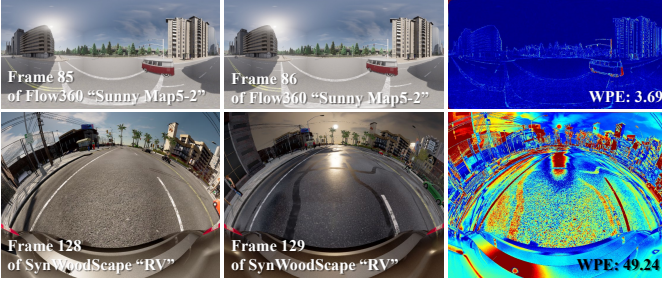


Fig. 7. Photoconsistency analysis of the dataset and heatmap visualization of WPE. Our Flow360 adheres to the photometric consistency principle of optical flow estimation, while the inconsistency of the sun’s pre-setting of SynWoodScape leads to drastic changes in lighting conditions, resulting in large errors in the interpolation results.

where  $\mathbf{x}$  is the pixel index and  $\mathbf{V}_{\text{GT}}$  is the ground-truth flow field. Obviously, the quality of the ground-truth flow is high when WPE is significantly lower than PE, *i.e.*, a high-quality optical flow field can convert one image to the next as much as possible [71]. We consider forward optical flow that results in a reduction in interpolation error of less than 10% to be medium/low-quality ground truth. We perform ground-truth quality analysis on the popular perspective optical flow dataset [32], [65], [69] and these three panorama datasets separately, and the results are shown in Tab. II. While the SynWoodScape dataset is also collected using CARLA, we discover that their interpolation errors are large. As shown in Fig. 7, this is due to the non-uniform pre-setting of the sun between the two frames during collecting process, *i.e.*, the dataset violates the principle of photometric consistency for optical flow estimation, resulting in drastic changes in lighting conditions. On the other hand, their acquisition frame rate is 10Hz, which makes the overlapping view area between frames smaller. Therefore, we consider that SynWoodScape is not suitable for evaluation. Compared to the public OmniFlowNet and our Flow360 datasets, the ground-truth flow of Replica360 dataset seems to be unreliable. Consequently, our quantitative evaluations are performed on the first two datasets.

## V. EXPERIMENTS

We conduct experiments using two typical learning-based flow method [19], [20] to verify the proposed PanoFlow framework. We confirm the role of the key components in PanoFlow through ablation experiments. For OmniFlowNet [22] and Yuan *et al.* [23], we use their official released codes for

testing. Unfortunately, neither the code nor the dataset of LiteFlowNet360 [50] is publicly available, therefore we cannot make a fair comparison with it. Since OmniFlowNet is an adaptive method designed for learning-based optical flow networks, we additionally upgrade its backbone from LiteFlowNet2 [48] to RAFT [19] and CSFlow [20] for quantitative experiments to demonstrate that our PanoFlow framework is more generic and effective. We further conduct qualitative comparisons on the public outdoor panoramic dataset OmniPhotos [29] and our PAL-collected panoramic videos.

### A. Training Details

Following previous works, we pretrain our model using the FlyingChairs [32]→FlyThings [69] schedule, followed by finetuning on our Flow360 dataset. We divide Flow360 into 5,000/1,400 image pairs for train/test subsets. Considering that the sunny days are the most common weather conditions, the test set of Flow360 covers sunny (57.1%), cloud (14.3%), fog (14.3%), and rain (14.3%). We train our model on an RTX 3090 GPU, implemented in PyTorch. We pretrain on FlyingChairs for 100k iterations with a batch size of 10, then train for 100k iterations on FlyingThings3D with a batch size of 6. Finally, we finetune on Flow360 with a batch size of 6 for another 100k iterations using the weights from the pretrained model. The ablation experiment is performed with 100k training iterations on Chairs, and the batch size is also 10. We time our method using an RTX 3090 GPU. The GRU iteration number is set to 12 during training and inference. We follow RAFT [19] for data augmentation. All experiments are with the same augmentations including occlusion augmentation [72], random rescale, perturbing brightness, as well as contrast-, saturation-, and hue augmentation.

### B. PanoFlow on Flow360

We evaluate PanoFlow on the Flow360 dataset using the test split. Results are shown in Tab. III, where we split the results based on the weather conditions. The best results are bolded, the second best are underlined. We term the method using the PanoFlow framework as PanoFlow (.). We denote \* and \*\* to distinguish models using FDA-R and FDA-E methods. C+T means that the models are trained on FlyingChairs (C) and FlyingThings (T). F indicates methods using only Flow360 (F) train split for finetuning. When using C+T for training, our method achieves an 11.7% error reduction for RAFT, and a 12.4% error reduction for CSFlow. The results of CSFlow are slightly better than RAFT, which demonstrates its better cross-dataset generalizability. After finetuning on Flow360, estimating flow under PanoFlow framework can further improve the accuracy. Our PanoFlow (CSFlow) improves EPE from 4.47 to 3.25 (↑27.3%). Interestingly, FDA-R also makes it easier for the model to cope with ERP deformations when trained on the perspective dataset. When we turn off FDA and train on Flow360, the FDA-E models have a slightly better overall accuracy than FDA-R, but this advantage does not hold in all weather conditions. We believe this is due to the fact that, by introducing deformed optical flow field for training, our model is able to extract robust features for computing visual similarity across different distortion modalities.



### C. Ablation Studies

To demonstrate the role of each core module in the proposed PanoFlow framework, we perform the ablation studies on Flow360 using the well-known RAFT structure [19]. We now describe the findings of each study.

TABLE III  
QUANTITATIVE RESULTS ON FLOW360 DATASET.  
\* DENOTES THE MODEL TRAINED WITH FDA-R.  
\*\* DENOTES THE MODEL TRAINED WITH FDA-E.

Training Data	Method	Sunny	Cloud	Fog	Rain	All (test)	Diff.
		EPE	EPE	EPE	EPE	EPE	
C+T	RAFT [19]	16.57	11.16	15.04	17.00	15.64	-
	PanoFlow (RAFT)*	14.93	11.25	13.88	13.36	14.03	↑ 10.3%
	PanoFlow (RAFT)**	<u>14.66</u>	<u>11.10</u>	<u>13.57</u>	<u>13.38</u>	<u>13.81</u>	↑ 11.7%
	CSFlow [20]	16.32	11.16	14.99	16.04	15.35	-
	PanoFlow (CSFlow)*	14.74	11.18	13.64	13.42	13.89	↑ 9.5%
	PanoFlow (CSFlow)**	<b>14.27</b>	<b>10.74</b>	<b>13.03</b>	<b>13.34</b>	<b>13.45</b>	↑ 12.4%
C+T+F	RAFT [19]	4.77	1.52	4.84	6.07	4.50	-
	PanoFlow (RAFT)*	3.62	<u>1.38</u>	3.60	4.25	3.39	↑ 24.7%
	PanoFlow (RAFT)**	3.58	1.41	3.63	4.17	3.36	↑ 25.3%
	CSFlow [20]	4.70	1.46	4.79	6.24	4.47	-
	PanoFlow (CSFlow)*	<u>3.56</u>	1.47	<b>3.56</b>	<b>3.94</b>	<u>3.31</u>	↑ 26.0%
	PanoFlow (CSFlow)**	<b>3.46</b>	<b>1.35</b>	<u>3.59</u>	<u>3.98</u>	<b>3.25</b>	↑ 27.3%

TABLE IV  
ABLATIONS ON FLOW DISTORTION AUGMENTATION.

Augmentation		Sunny	Cloud	Fog	Rain	All (test)
FDA-R	FDA-E					
-	-	18.53	12.88	17.00	18.02	17.43
✓	-	17.86	12.63	16.60	17.59	16.89
-	✓	<b>16.65</b>	<b>11.67</b>	<b>15.48</b>	<b>16.50</b>	<b>15.75</b>

TABLE V  
ABLATIONS ON CORE COMPONENTS OF PANOFLOW.

Core Components			Sunny	Cloud	Fog	Rain	All (Test)
FDA-E	CFE	DCN					
-	-	-	18.53	12.88	17.00	18.02	17.43
✓	-	-	16.65	11.67	15.48	16.50	15.75
-	✓	-	16.56	12.46	15.25	15.35	15.62
-	-	✓	18.11	12.69	16.66	17.78	17.08
-	✓	✓	15.93	12.13	14.69	15.03	15.08
✓	-	✓	16.44	11.41	15.25	16.07	15.50
✓	✓	-	14.72	11.28	13.69	13.84	13.96
✓	✓	✓	<b>14.55</b>	<b>11.09</b>	<b>13.57</b>	<b>13.42</b>	<b>13.75</b>

TABLE VI  
CYCLIC FLOW ESTIMATION ABLATION.

CFE Settings	Flow360 (test)				Avg.	Diff.	Latency
	sunny	cloud	fog	rain			
Baseline	4.77	1.52	4.84	6.07	4.50	-	<b>0.10s</b>
Circular Convolution	5.72	2.73	6.02	7.50	5.59	↓ 19.5%	0.11s
Double Estimation	3.81	1.68	3.86	4.29	3.58	↑ 20.4%	0.18s
Half Zero Padding	3.82	1.54	3.74	4.57	3.59	↑ 20.2%	0.24s
Half Same Padding	31.5	23.5	22.1	35.8	29.6	↓ 558%	0.13s
Default	<b>3.58</b>	<b>1.41</b>	<b>3.63</b>	<b>4.17</b>	<b>3.36</b>	↑ 25.3%	0.13s

**Flow Distortion Augmentation:** We explore the role of two different flow distortion variants on the model’s ability to

adapt from pinhole to panoramic domains. The results are shown in Tab. IV. Both FDA-R and FDA-E can help models to overcome ERP deformation, which indicate that distorted optical flow is beneficial for the model to learn robust features. Although the total number of effectively supervised pixels is reduced in FDA-E, its modality is closer to ERP, thus the model using FDA-E gains an advantage. In the following ablation experiments, we use the FDA-E model by default.

**Core Components:** Tab. V shows how performance varies as each core component (FDA-E: flow distortion augmentation in ERP format; CFE: cyclic flow estimation; DCN: deformable receptive field encoder) of our model is removed. We can see that every component contributes to the overall performance. We find that CFE has the greatest impact on accuracy. The result is surprising, considering that this method that can be used without any retraining. This also reveals that the PanoFlow framework can easily benefit from advances in general optical flow networks. When all the key components are in place, the model performs optimally in all weathers. In the following experiments, we use the “full” version of our method (last row of Tab. V).

**Cyclic Flow Estimation:** We additionally conduct an ablation study based on PanoFlow (RAFT) that has been finetuned on Flow360 to further investigate how the setting of the CFE affects the accuracy and efficiency. Tab. VI shows that CFE improves the performance the most in the default setting.

**Circular Convolution:** In order to explore the ability of circular convolution to capture large-displacement cyclic visual similarity, we replace the convolutional layers in the model with circular convolutions, where experimental results show they do not help performance. We believe that this is because the circular convolution uses a simple padding operation to warp the image, and the introduced cyclicity is insufficient, considering that the end point of the 360° optical flow may fall within the area  $[0, \frac{W}{2}]$  outside the left and right boundaries of the panoramic image. However, most of the flow vectors are still given in the direction of the traditional optical flow, which makes it a disadvantage in 360° flow estimation (↓19.5%). **Double Estimation:** A naive idea is to swap the left and right regions directly, estimate twice and take the respective minimum values. This does improve the accuracy, but the time complexity is also doubled. It also confuses the model during encoding the false image boundary introduced by the swap operation. **Half Zero Padding:** Based on the above observations, we naturally associate whether the another region’s feature will interfere with the results of the region of interest when decoding. Thus, we try replacing half of the feature maps with empty tensors, resulting in one encoding and four decodings. We find that it has no advantages over the default setting. **Half Same Padding:** We further replace the zero feature with same feature of the region of interest. The same features make the model face two confusing scene cues at the same time when calculating the visual similarity, which leads to terrible performance regression. **Default:** The performance improvement brought by CFE is the most significant in the default setting, and its time complexity is only modest.

We further explore the horizontal distribution of the gain introduced by CFE. As shown in Fig. 8, CFE improves the

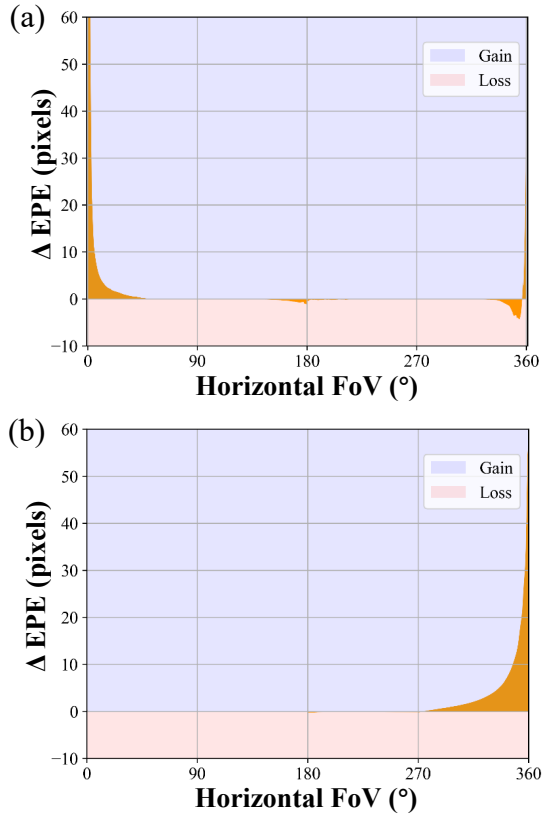


Fig. 8. The distribution of the optical flow estimation EPE variation with the horizontal FoV introduced by the CFE method. (a) Statistical results on Flow360 test split, (b) Statistical results on the OmniFlowNet dataset.

model’s ability to cope with cross-boundary optical flow, which is an essential difficult part of panoramic flow estimation. On Flow360, CFE seems to cause a slight degradation near the right boundary, which we believe is due to the fact that the road features of Flow360 are highly similar, causing the model to confuse the road on both sides of the boundary during cyclic inference. And our virtual collection vehicle goes straight ahead, resulting in less cross-boundary optical flow. On the OmniFlowNet dataset, it can be observed that the accuracy is significantly improved in the range of  $270^\circ \sim 360^\circ$  in FoV. This is reasonable because the dataset only contains forward- and rightward movements, and the crossing of boundaries generally occurs on the right side of the image. Considering real-world cases, the vehicle cannot move completely straight ahead along the lane line, and traffic accidents might occur when the vehicle turns, thus, CFE is ideally suitable for real driving scenarios.

#### D. Comparison with the State-of-the-Art

**Quantitative Comparison on Synthetic Data:** OmniFlowNet [22] is a state-of-the-art CNN for optical flow estimation in omnidirectional images which can be built on general CNNs for perspective images. We reproduce the OmniFlowNet using MMFlow [73] and compare it with our model. Since OmniFlowNet is built on LiteFlowNet2 [48], which is inconsistent to our baseline, we also apply the architecture of OmniFlowNet to RAFT and CSFlow. We evaluate the models on the OmniFlowNet dataset [22] and our Flow360 dataset as

TABLE VII  
COMPARISON WITH STATE-OF-THE-ART.  
—ft DENOTES THE MODEL FINE-TUNED ON FLOW360

Method	OmniFlowNet Dataset					Flow360 (test)		Latency
	Cart.	Forest	Poly.	Avg.	Diff.	Avg.	Diff.	
OmniFlowNet [22]	5.37	8.68	7.32	7.12	-	22.16	-	0.02s
Yuan <i>et al.</i> [23]	9.13	14.27	10.22	11.21	↓ 57.4%	20.35	↑ 8.17%	10.48s
OmniFlowNet (RAFT)	4.84	8.70	6.74	6.76	↑ 5.06%	19.61	↑ 11.5%	0.43s
OmniFlowNet (CSFlow)	4.74	8.66	6.52	6.64	↑ 6.74%	19.47	↑ 12.1%	0.44s
OmniFlowNet (RAFT)-ft	3.55	7.28	5.28	5.37	↑ 24.6%	14.33	↑ 35.3%	0.43s
OmniFlowNet (CSFlow)-ft	3.57	7.21	5.50	5.43	↑ 23.7%	15.33	↑ 30.8%	0.44s
PanoFlow (RAFT)*	3.95	4.77	6.78	5.17	↑ 27.4%	14.03	↑ 36.7%	0.13s
PanoFlow (RAFT)**	2.71	4.14	5.29	4.05	↑ 43.1%	13.81	↑ 37.7%	0.13s
PanoFlow (RAFT)*-ft	2.31	3.53	4.91	3.58	↑ 49.8%	3.39	↑ 84.7%	0.13s
PanoFlow (RAFT)**-ft	<b>1.97</b>	<b>3.29</b>	<b>4.24</b>	<b>3.17</b>	↑ 55.5%	<b>3.36</b>	↑ 84.8%	0.13s
PanoFlow (CSFlow)*	3.81	4.76	6.92	5.16	↑ 27.5%	13.89	↑ 37.3%	0.14s
PanoFlow (CSFlow)**	2.83	4.58	5.57	4.33	↑ 39.2%	13.45	↑ 39.3%	0.14s
PanoFlow (CSFlow)*-ft	2.02	<b>3.51</b>	4.48	3.34	↑ 53.1%	3.31	↑ 85.1%	0.14s
PanoFlow (CSFlow)**-ft	<b>1.92</b>	3.53	<b>4.37</b>	<b>3.27</b>	↑ 54.1%	<b>3.25</b>	↑ 85.3%	0.14s

shown in Tab. VII. All models are trained on FlyingChairs (C) + FlyThings (T), with “-ft” indicating that the model was additionally fine-tuned on the Flow360 data. We also report the accuracy of the icosahedron tangent-plane panoramic flow estimation method [23] on both datasets.

When the method of OmniFlowNet is applied to RAFT (OmniFlowNet (RAFT)), the results are improved to some extent (↑5.1% on the OmniFlowNet dataset). However, PanoFlow (RAFT)\*\* improves the performance significantly (↑43.1% on the OmniFlowNet dataset). After finetuning on Flow360, the accuracy of both networks are further improved, indicating that the Flow360 dataset is effective for panoramic optical flow tasks. When training with FDA-R, PanoFlow (CSFlow)\*-ft achieves better performance than PanoFlow (RAFT)\*-ft on both datasets, which proves that our CSFlow structure is better at learning robust features across different distortion modalities. PanoFlow (CSFlow)\*\*-ft ranks 1st on our Flow360 dataset (3.25 pixels), while PanoFlow (RAFT)\*\*-ft gives better results on the OmniFlowNet dataset (3.17 pixels), which we believe is due to the domain gap between the two datasets. On the OmniFlowNet dataset, our approach achieves a 55.5% error reduction than the current state-of-the-art panoramic flow method. On Flow360, PanoFlow also outperforms OmniFlowNet by a large margin, dramatically decreasing EPE from 22.16 to 3.25, while maintaining high efficiency (0.14s).

We present the error heatmap analysis on both datasets in Fig 9. Although the convolution kernel adopts a fixed ERP deformation, OmniFlowNet [22] still has difficulties in dealing with high-latitude distortion. This defect is especially pronounced on Flow360, since our dataset considers both foreground- and background panoramic optical flow, while OmniFlowNet dataset only gives foreground ground-truth flow. On the other hand, when the pre-trained RAFT is converted to OmniFlowNet (RAFT), we observe mosaic-like estimation errors in the high-latitude regions of the ERP, indicating the

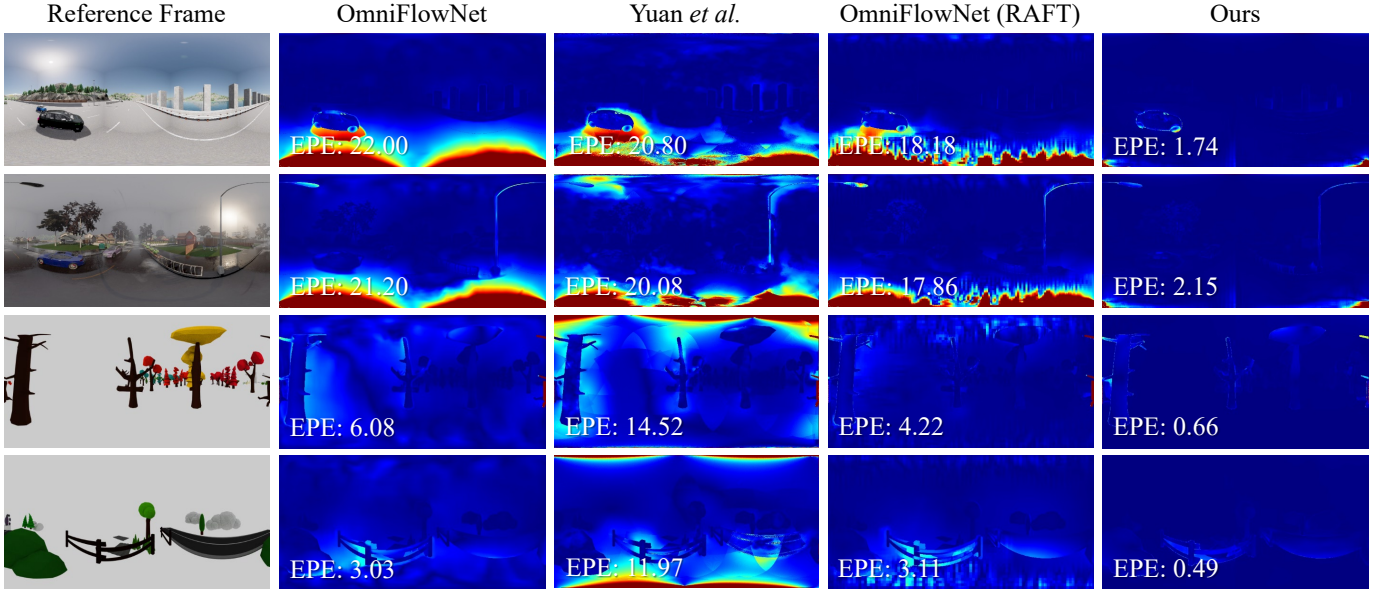


Fig. 9. Error heatmap visualizations on Flow360 test split and OmniFlowNet datasets [22]. PanoFlow can easily cope with the challenges introduced by image distortion in high-latitude regions and provide a clear and smooth panoramic flow field in one shot.

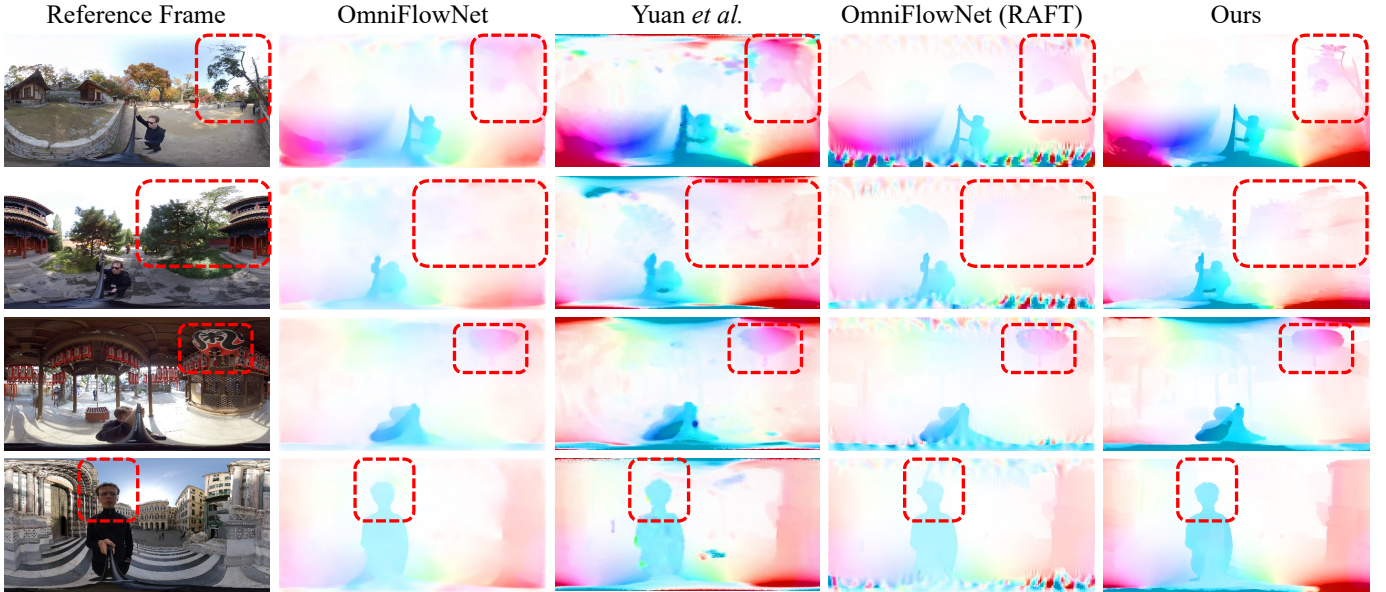


Fig. 10. Qualitative results on the OmniPhotos [29] dataset. PanoFlow successfully generalizes from synthetic dataset to real scenes, and the panoramic flow field visualizations are clean and discriminative while well preserving the details of the image.

insufficient generality of the OmniFlowNet method. Since Yuan *et al.* estimate the panoramic flow on both the icosahedron and the cubemap multiple times, the results tend to appear many tangent plane boundaries. Thanks to our FDA and deformable receptive field encoders, PanoFlow can easily handle high-latitude deformation of ERP. Noticeably, applying CFE produces a large improvement near the boundary, which is an essential difficult part of  $360^\circ$  flow estimation (see the third row of Fig 9).

**Qualitative Comparisons in the Real World:** Considering that the ground truth of dense flow field in the real world is almost impossible to obtain [65], [69], we qualitatively compare the flow on both the public OmniPhotos dataset [29] without the ground truth and the PAL video stream collected by ourselves to verify the synthetic-to-real generalization ability of PanoFlow. As shown in Fig 10, PanoFlow gives high-quality

dense optical flow in real scenes. Regarding OmniFlowNet and Yuan *et al.*, they suffer from limited distortion-aware capacity, thus being not accurate enough in the real-world domain. Although we additionally upgrade the backbone of OmniFlowNet to RAFT, its ability to capture large displacements is still insufficient compared with our method. OmniFlowNet (RAFT) also exhibits mosaic-like errors again in the real scene, proving the lack of generality of the method. Moreover, PanoFlow is able to capture adequate details of real-world images, which is evidently better than previous works.

To further investigate the practical performance of the proposed PanoFlow solution on real data, we install a panoramic annular lens (PAL) system with an FoV of  $60^\circ \times 360^\circ$  on top of a mobile robot (see Fig. 12), which navigates around the campus according to the remote control. As shown in Fig. 11, we collect panoramic videos of campus street scenes





Fig. 11. Qualitative comparison of existing methods in outdoor-campus 360° image sequences that captured by our PAL camera. PanoFlow gives optical flow with clear and sharp boundaries for both foreground and background, which means stronger generalization ability for the real-world.



(a) Mobile Robot

(b) PAL Camera

Fig. 12. (a) Our outdoor mobile robot is equipped with a Panoramic Annular Lens (PAL) camera and a laptop. (b) PAL for capturing outdoor panoramic video streams.

and compare our approach with the results given by OmniFlowNet [22] and the method from Yuan *et al.* [23]. Although the robot’s perspective and FoV are significantly different to that of the virtual camera used in the Flow360 for training, PanoFlow still gives clear and sharp optical flow estimation. For other methods, estimating directly on PAL images will lead to epic failures. Therefore, we convert the PAL video stream to the standard ERP format with an aspect ratio of 2:1 before estimation for each method except PanoFlow. This also reveals that these methods will face additional computational overhead when used on real panoramic shots, as their methods are only designed for complete ERP data. Specifically, for pedestrian and fast-moving vehicles in the foreground of panoramic images, PanoFlow does not confuse them with the motion of the background, even if they are deformed to varying degrees. Edges are blurred and indistinguishable in OmniFlowNet’s background flow estimation, whereas the outlines of street scenes are still sharp and recognizable in PanoFlow’s results. Compared with the method proposed by Yuan *et al.*, PanoFlow gives optical flow with better continuity, and the detailed features are also well preserved. We conclude that our method outperforms the previous state-of-the-art work for both foreground and background, showing excellent synthetic-to-real generalizability.

TABLE VIII  
RUNNING TIME, PARAMETERS, AND MEMORY REQUIREMENT.

Method	Parameters	GPU Memory	Time	$\Delta$ Accuracy
RAFT [19]	5.3M	2.67GB	0.10s	-
PanoFlow (RAFT)*	5.3M	2.78GB	0.13s	$\uparrow$ 24.7%
PanoFlow (RAFT)**	5.3M	2.78GB	0.13s	$\uparrow$ 25.3%
CSFlow [20]	5.6M	3.42GB	0.10s	-
PanoFlow (CSFlow)*	5.6M	4.04GB	0.14s	$\uparrow$ 26.0%
PanoFlow (CSFlow)**	5.6M	4.04GB	0.14s	$\uparrow$ 27.3%



Fig. 13. The failure case of PanoFlow. When there is overexposure and lack of texture near the middle of the panorama, CFE may incur difficulty distinguishing features on both sides, resulting in reduced optical flow continuity near the middle of the estimation results.

### E. Efficiency Analysis

We report the parameter counts, memory requirements during inference, inference time, and the accuracy performance as shown in Tab. VIII. Accuracy is determined by the performance on the Flow360 (test) after training on C+T+F. The image size is  $512 \times 1024$ . RAFT takes 2.67GB memory while our approach takes 2.78GB memory. Due to the additional global context introduced by the decoder in CSFlow, the memory consumption of PanoFlow (CSFlow) is larger than the former. Overall, the results demonstrate that the computational overhead of PanoFlow is low, in contrast to the significant performance improvement, and is therefore suitable for intelligent vehicles to perceive surrounding temporal cues.

## F. Failure Case Analysis

As shown in Fig. 13, when there is overexposure in the middle area of the image, the optical flow continuity on both sides will be reduced during cyclic estimation, which is reasonable because the features on both sides become difficult to distinguish and confuse the decoder of the optical flow network. Overcoming this limitation requires some form of supervision or better backbones, *e.g.*, reasoning about panoramic semantics, reasoning about spatio-temporal features in video, or reasoning about fusion with high dynamic range sensors, such as event cameras. Future work can be dedicated to transferring our method to these approaches.

## VI. CONCLUSION

In this paper, we proposed PanoFlow, a flexible framework for estimating 360° optical flow using flow distortion augmentation, cyclic flow estimation, and deformable receptive filed encoder. We also proposed Flow360, a publicly available synthetic panoramic optical flow dataset, which can be used for training and evaluation. We have proved through a large number of quantitative experiments that our PanoFlow is compatible with any optical flow methods of an encoder-decoder structure, which significantly improves the accuracy of panoramic flow estimation while ensuring computational efficiency. PanoFlow achieves state-of-the-art performance on both public OmniFlowNet dataset and our Flow360. PanoFlow also demonstrates strong synthetic-to-real generalizability in the real world, giving high-quality panoramic flow fields. We look forward to further exploring the adaptability of the PanoFlow framework for other downstream panoramic tasks.

In the future, we aim to explore other panoramic scene understanding tasks, such as the fusion of panoramic camera and LiDAR sensor for an entire and complete semantic and temporal surrounding perception. We also have the intention to look into 3D scene flow estimation based on panoramic cameras. In addition to panoramic cameras with ultra-wide FoV, we are also interested in exploring optical flow estimation for event cameras with ultra-high dynamic range.

## REFERENCES

- [1] G. Wang, C. Zhang, H. Wang, J. Wang, Y. Wang, and X. Wang, "Unsupervised learning of depth, optical flow and pose with occlusion from 3D geometry," *IEEE Transactions on Intelligent Transportation Systems*, vol. 23, no. 1, pp. 308–320, 2022.
- [2] H. Liu, T. Lu, Y. Xu, J. Liu, W. Li, and L. Chen, "CamLiFlow: Bidirectional camera-LiDAR fusion for joint optical flow and scene flow estimation," in *Proc. CVPR*, 2022, pp. 5791–5801.
- [3] V. Brebion, J. Moreau, and F. Davoine, "Real-time optical flow for vehicular perception with low-and high-resolution event cameras," *IEEE Transactions on Intelligent Transportation Systems*, 2021.
- [4] G. Wang, S. Ren, and H. Wang, "Unsupervised learning of optical flow with non-occlusion from geometry," *IEEE Transactions on Intelligent Transportation Systems*, 2022.
- [5] J. Fang, J. Qiao, J. Bai, H. Yu, and J. Xue, "Traffic accident detection via self-supervised consistency learning in driving scenarios," *IEEE Transactions on Intelligent Transportation Systems*, 2022.
- [6] K. Yang, J. Zhang, S. Reiß, X. Hu, and R. Stiefelhagen, "Capturing omni-range context for omnidirectional segmentation," in *Proc. CVPR*, 2021, pp. 1376–1386.
- [7] R. Gadde, V. Jampani, and P. V. Gehler, "Semantic video CNNs through representation warping," in *Proc. ICCV*, 2017, pp. 4463–4472.
- [8] N. Hirose, F. Xia, R. Martín-Martín, A. Sadeghian, and S. Savarese, "Deep visual MPC-policy learning for navigation," *IEEE Robotics and Automation Letters*, vol. 4, no. 4, pp. 3184–3191, 2019.
- [9] D. Caruso, J. Engel, and D. Cremers, "Large-scale direct SLAM for omnidirectional cameras," in *Proc. IROS*, 2015, pp. 141–148.
- [10] X. Zhu, Y. Xiong, J. Dai, L. Yuan, and Y. Wei, "Deep feature flow for video recognition," in *Proc. CVPR*, 2017, pp. 4141–4150.
- [11] Z. Min, Y. Yang, and E. Dunn, "VOLDOR: Visual odometry from log-logistic dense optical flow residuals," in *Proc. CVPR*, 2020, pp. 4897–4908.
- [12] Z. Teed and J. Deng, "DROID-SLAM: Deep visual SLAM for monocular, stereo, and RGB-D cameras," in *Proc. NeurIPS*, 2021, pp. 16558–16569.
- [13] S. Gao, K. Yang, H. Shi, K. Wang, and J. Bai, "Review on panoramic imaging and its applications in scene understanding," *arXiv preprint arXiv:2205.05570*, 2022.
- [14] L. Chen *et al.*, "Surrounding vehicle detection using an FPGA panoramic camera and deep CNNs," *IEEE Transactions on Intelligent Transportation Systems*, vol. 21, no. 12, pp. 5110–5122, 2020.
- [15] R. Liu, G. Zhang, J. Wang, and S. Zhao, "Cross-modal 360° depth completion and reconstruction for large-scale indoor environment," *IEEE Transactions on Intelligent Transportation Systems*, 2022.
- [16] A. Petrovai and S. Nedevschi, "Semantic cameras for 360-degree environment perception in automated urban driving," *IEEE Transactions on Intelligent Transportation Systems*, 2022.
- [17] J. S. Berrio, M. Shan, S. Worrall, and E. Nebot, "Camera-LiDAR integration: Probabilistic sensor fusion for semantic mapping," *IEEE Transactions on Intelligent Transportation Systems*, 2021.
- [18] D. Sun, X. Yang, M.-Y. Liu, and J. Kautz, "PWC-net: CNNs for optical flow using pyramid, warping, and cost volume," in *Proc. CVPR*, 2018, pp. 8934–8943.
- [19] Z. Teed and J. Deng, "RAFT: Recurrent all-pairs field transforms for optical flow," in *Proc. ECCV*, vol. 12347, 2020, pp. 402–419.
- [20] H. Shi, Y. Zhou, K. Yang, X. Yin, and K. Wang, "CSFlow: Learning optical flow via cross strip correlation for autonomous driving," in *Proc. IV*, 2022.
- [21] N. Zioulis, A. Karakottas, D. Zarpalas, and P. Daras, "OmniDepth: Dense depth estimation for indoors spherical panoramas," in *Proc. ECCV*, vol. 11210, 2018, pp. 453–471.
- [22] C.-O. Artiz, H. Zhang, G. Allibert, and C. Demonceaux, "OmniFlowNet: a perspective neural network adaptation for optical flow estimation in omnidirectional images," in *Proc. ICPR*, 2021, pp. 2657–2662.
- [23] M. Yuan and C. Richardt, "360° optical flow using tangent images," in *Proc. BMVC*, 2021.
- [24] K. Yang, X. Hu, L. M. Bergasa, E. Romera, and K. Wang, "PASS: Panoramic annular semantic segmentation," *IEEE Transactions on Intelligent Transportation Systems*, vol. 21, no. 10, pp. 4171–4185, 2020.
- [25] K. Yang, X. Hu, H. Chen, K. Xiang, K. Wang, and R. Stiefelhagen, "DS-PASS: Detail-sensitive panoramic annular semantic segmentation through SwaftNet for surrounding sensing," in *Proc. IV*, 2020, pp. 457–464.
- [26] J. Dai *et al.*, "Deformable convolutional networks," in *Proc. ICCV*, 2017, pp. 764–773.
- [27] A. Dosovitskiy, G. Ros, F. Codevilla, A. Lopez, and V. Koltun, "CARLA: An open urban driving simulator," in *Proc. CoRL*, vol. 78, 2017, pp. 1–16.
- [28] A. R. Sekkat *et al.*, "SynWoodScape: Synthetic surround-view fisheye camera dataset for autonomous driving," *IEEE Robotics and Automation Letters*, 2022.
- [29] T. Bertel, M. Yuan, R. Lindroos, and C. Richardt, "OmniPhotos: casual 360° VR photography," *ACM Transactions on Graphics (TOG)*, vol. 39, no. 6, pp. 1–12, 2020.
- [30] B. K. Horn and B. G. Schunck, "Determining optical flow," *Artificial Intelligence*, vol. 17, no. 1-3, pp. 185–203, 1981.
- [31] B. D. Lucas and T. Kanade, "An iterative image registration technique with an application to stereo vision," in *Proc. IJCAI*, 1981, pp. 674–679.
- [32] A. Dosovitskiy *et al.*, "FlowNet: Learning optical flow with convolutional networks," in *Proc. ICCV*, 2015, pp. 2758–2766.
- [33] D. Tran, L. Bourdev, R. Fergus, L. Torresani, and M. Paluri, "Deep End2End Voxel2Voxel prediction," in *Proc. CVPRW*, 2016, pp. 402–409.
- [34] A. Ahmadi and I. Patras, "Unsupervised convolutional neural networks for motion estimation," in *Proc. ICIP*, 2016, pp. 1629–1633.
- [35] J. Wulff and M. J. Black, "Efficient sparse-to-dense optical flow estimation using a learned basis and layers," in *Proc. CVPR*, 2015, pp. 120–130.

- [36] F. Zhang, O. J. Woodford, V. Prisacariu, and P. H. S. Torr, "Separable flow: Learning motion cost volumes for optical flow estimation," in *Proc. ICCV*, 2021, pp. 10 787–10 797.
- [37] S. Jiang, D. Campbell, Y. Lu, H. Li, and R. Hartley, "Learning to estimate hidden motions with global motion aggregation," in *Proc. ICCV*, 2021, pp. 9752–9761.
- [38] S. Zhao, L. Zhao, Z. Zhang, E. Zhou, and D. Metaxas, "Global matching with overlapping attention for optical flow estimation," in *Proc. CVPR*, 2022, pp. 17 592–17 601.
- [39] S. Bai, Z. Geng, Y. Savani, and J. Z. Kolter, "Deep equilibrium optical flow estimation," in *Proc. CVPR*, 2022, pp. 620–630.
- [40] A. Luo, F. Yang, X. Li, and S. Liu, "Learning optical flow with kernel patch attention," in *Proc. CVPR*, 2022, pp. 8906–8915.
- [41] Z. Zheng *et al.*, "DIP: Deep inverse patchmatch for high-resolution optical flow," in *Proc. CVPR*, 2022, pp. 8925–8934.
- [42] X. Sui *et al.*, "CRAFT: Cross-attentional flow transformer for robust optical flow," in *Proc. CVPR*, 2022, pp. 17 602–17 611.
- [43] H. Xu, J. Zhang, J. Cai, H. Rezatofighi, and D. Tao, "GMFlow: Learning optical flow via global matching," in *Proc. CVPR*, 2022, pp. 8121–8130.
- [44] J. Jeong, J. M. Lin, F. Porikli, and N. Kwak, "Imposing consistency for optical flow estimation," in *Proc. CVPR*, 2022, pp. 3181–3191.
- [45] P. Liu, M. Lyu, I. King, and J. Xu, "SelfFlow: Self-supervised learning of optical flow," in *Proc. CVPR*, 2019, pp. 4571–4580.
- [46] H.-Y. Tung, H.-W. Tung, E. Yumer, and K. Fragkiadaki, "Self-supervised learning of motion capture," *Proc. NeurIPS*, pp. 5236–5246, 2017.
- [47] E. Ilg, N. Mayer, T. Saikia, M. Keuper, A. Dosovitskiy, and T. Brox, "FlowNet 2.0: Evolution of optical flow estimation with deep networks," in *Proc. CVPR*, 2017, pp. 1647–1655.
- [48] T.-W. Hui, X. Tang, and C. C. Loy, "A lightweight optical flow CNN - Revisiting data fidelity and regularization," *IEEE Transactions on Pattern Analysis and Machine Intelligence*, vol. 43, no. 8, pp. 2555–2569, 2021.
- [49] Z. Huang, X. Shi, C. Zhang, Q. Wang, K. C. Cheung, H. Qin, J. Dai, and H. Li, "FlowFormer: A transformer architecture for optical flow," *arXiv preprint arXiv:2203.16194*, 2022.
- [50] K. Bhandari, Z. Zong, and Y. Yan, "Revisiting optical flow estimation in 360 videos," in *Proc. ICPR*, 2021, pp. 8196–8203.
- [51] S. Im, H. Ha, F. Rameau, H.-G. Jeon, G. Choe, and I. S. Kweon, "All-around depth from small motion with a spherical panoramic camera," in *Proc. ECCV*, vol. 9907, 2016, pp. 156–172.
- [52] H. Jiang, Z. Sheng, S. Zhu, Z. Dong, and R. Huang, "UniFuse: Uni-directional fusion for 360° panorama depth estimation," *IEEE Robotics and Automation Letters*, vol. 6, no. 2, pp. 1519–1526, 2021.
- [53] C. Sun, M. Sun, and H.-T. Chen, "HoHoNet: 360 indoor holistic understanding with latent horizontal features," in *Proc. CVPR*, 2021, pp. 2573–2582.
- [54] J. Zhang, K. Yang, C. Ma, S. Reiß, K. Peng, and R. Stiefelhagen, "Bending reality: Distortion-aware transformers for adapting to panoramic semantic segmentation," in *Proc. CVPR*, 2022, pp. 16 917–16 927.
- [55] L. Deng, M. Yang, H. Li, T. Li, B. Hu, and C. Wang, "Restricted deformable convolution-based road scene semantic segmentation using surround view cameras," *IEEE Transactions on Intelligent Transportation Systems*, vol. 21, no. 10, pp. 4350–4362, 2020.
- [56] A. Jaus, K. Yang, and R. Stiefelhagen, "Panoramic panoptic segmentation: Insights into surrounding parsing for mobile agents via unsupervised contrastive learning," *arXiv preprint arXiv:2206.10711*, 2022.
- [57] I. Armeni, S. Sax, A. R. Zamir, and S. Savarese, "Joint 2D-3D-semantic data for indoor scene understanding," *arXiv preprint arXiv:1702.01105*, 2017.
- [58] J. Zhang, C. Ma, K. Yang, A. Roitberg, K. Peng, and R. Stiefelhagen, "Transfer beyond the field of view: Dense panoramic semantic segmentation via unsupervised domain adaptation," *IEEE Transactions on Intelligent Transportation Systems*, vol. 23, no. 7, pp. 9478–9491, 2022.
- [59] Y. Liao, J. Xie, and A. Geiger, "KITTI-360: A novel dataset and benchmarks for urban scene understanding in 2D and 3D," *IEEE Transactions on Pattern Analysis and Machine Intelligence*, 2022.
- [60] S. Yogamani *et al.*, "WoodScape: A multi-task, multi-camera fisheye dataset for autonomous driving," in *Proc. ICCV*, 2019, pp. 9307–9317.
- [61] A. R. Sekkat, Y. Dupuis, P. Vasseur, and P. Honeine, "The OmniScape dataset," in *Proc. ICRA*, 2020, pp. 1603–1608.
- [62] J. Mei *et al.*, "Waymo open dataset: Panoramic video panoptic segmentation," in *Proc. ECCV*, 2022.
- [63] R. Seidel, A. Apitzsch, and G. Hirtz, "OmniFlow: Human omnidirectional optical flow," in *Proc. CVPRW*, 2021, pp. 3678–3681.
- [64] J. Straub *et al.*, "The replica dataset: A digital replica of indoor spaces," *arXiv preprint arXiv:1906.05797*, 2019.
- [65] D. J. Butler, J. Wulff, G. B. Stanley, and M. J. Black, "A naturalistic open source movie for optical flow evaluation," in *Proc. ECCV*, vol. 7577, 2012, pp. 611–625.
- [66] S. Baker, D. Scharstein, J. Lewis, S. Roth, M. J. Black, and R. Szeliski, "A database and evaluation methodology for optical flow," *International Journal of Computer Vision*, vol. 92, no. 1, pp. 1–31, 2011.
- [67] A. Geiger, P. Lenz, C. Stiller, and R. Urtasun, "Vision meets robotics: The KITTI dataset," *The International Journal of Robotics Research*, vol. 32, no. 11, pp. 1231–1237, 2013.
- [68] D. Kondermann *et al.*, "The HCI benchmark suite: Stereo and flow ground truth with uncertainties for urban autonomous driving," in *Proc. CVPRW*, 2016, pp. 19–28.
- [69] N. Mayer *et al.*, "A large dataset to train convolutional networks for disparity, optical flow, and scene flow estimation," in *Proc. CVPR*, 2016, pp. 4040–4048.
- [70] H. Xu, J. Yang, J. Cai, J. Zhang, and X. Tong, "High-resolution optical flow from 1D attention and correlation," in *Proc. ICCV*, 2021, pp. 10 478–10 487.
- [71] B. McCane, K. Novins, D. Crannitch, and B. Galvin, "On benchmarking optical flow," *Computer Vision and Image Understanding*, vol. 84, no. 1, pp. 126–143, 2001.
- [72] G. Yang, J. Manela, M. Happold, and D. Ramanan, "Hierarchical deep stereo matching on high-resolution images," in *Proc. CVPR*, 2019, pp. 5515–5524.
- [73] M. Contributors, "MMFlow: OpenMMLab optical flow toolbox and benchmark," <https://github.com/open-mmlab/mmlflow>, 2021.